Numerical Heat Transfer, Part B, 58: 262–286, 2010

ISSN: 1040-7790 print/1521-0626 online
DOI: 10.1080/10407790.2010.511969

Taylor & Francis
Taylor & Francis Group

DEVELOPMENT OF AN INCOMPRESSIBLE NAVIER-STOKES SOLVER INVOLVING SYMPLECTIC AND NONSYMPLECTIC TIME INTEGRATORS

Tony W. H. Sheu[1,2,3] and C. H. Yu[1]

[1]*Department of Engineering Science and Ocean Engineering, National Taiwan University, Taipei, Taiwan, Republic of China*

[2]*Taida Institute of Mathematical Sciences (TIMS), National Taiwan University, Taipei, Taiwan, Republic of China*

[3]*Center for Quantum Science and Engineering (CQSE), National Taiwan University, Taipei, Taiwan, Republic of China*

This article develops a heat/flow solver for properly simulating incompressible viscous flow at high Reynolds numbers and natural-convection flow at high Rayleigh numbers. Our strategy of simulating these problems is to retain some rich geometric properties embedded in the invisid Euler equations. Thanks to the underlying theory of Clebsch velocity decomposition, which divides the velocity vector as the sum of three velocity components due to the potential, rotational, and viscous contributions, the mixed-type Navier-Stokes equations cast in primitive variables can be fractionally split into three corresponding equations which are coupled to each other. In the pure advection step, the symplectic Runge-Kutta integrator is employed to approximate the temporal derivative term so as to numerically retain the Hamiltonians embedded in the lossless Euler differential equations. In addition, an upwinding scheme with minimized phase error is applied to discretize the first-order spatial derivative terms. In the diffusion step, we approximate the time derivative term shown in the time-dependent parabolic equation using a time-stepping scheme which does not need to be symplectic and is thus different from that used in the first step for the calculation of Euler solutions. We then solve the velocity vector from the projection step, subject to the divergence-free constraint condition. The proposed method is validated through benchmark tests. The predicted results of the incompressible Navier-Stokes and natural-convection equations are also justified for the problems investigated at high Reynolds and high Rayleigh numbers, respectively.

INTRODUCTION

In addition to the difficult issues associated with stability and accuracy in truly multidimensional incompressible viscous flow simulations, a proper specification of boundary conditions, in particular for problems when solid walls are present, remains not fully clear [1]. The objective of this article is to develop a numerically

Received 27 November 2009; accepted 14 July 2010.

This work was supported by the National Science Council of the Republic of China under Grants NSC-94-2611-E-002-021 and NSC-94-2745-P-002-002.

Address correspondence to Tony W. H. Sheu, Department of Engineering Science and Ocean Engineering, National Taiwan University, No. 1, Sec. 4, Roosevelt Road, Taipei, Taiwan 106, Republic of China. E-mail: twhsheu@ntu.edu.tw

NOMENCLATURE

$a_1, c_1 - c_3, b_1 - b_3$	coefficients in Eq. (24)	Ra	Rayleigh number
$\bar{a}_1, \bar{c}_1 - \bar{c}_3, \bar{b}_1 - \bar{b}_3$	coefficients in Eq. (25)	Re	Reynolds number
C_v	specific heat at constant volume	s	Entropy
		$\underline{u}$	velocity vector
E	kinetic energy	$\bar{\alpha}$	actual wave number
h	grid size	$\tilde{\alpha}$	effective wave number
H	Hamiltonian	γ	specific heat ratio
H_e	helicity	λ^i	Clebsch variable
$\overline{\mathrm{Nu}}$	averaged Nusselt number	μ^i	Clebsch variable
Nu_x	local Nusselt number	ϕ	scalar function
p	pressure	ω_e	vortex strength
Q	local heat flux	Ω	enstrophy

stable and long-time-accurate method, which follows the rigorous theory, such that the developed method for solving the incompressible Navier-Stokes equations possesses a certain generality. Our strategy is to approximate the temporal and spatial derivatives as faithfully as possible. Furthermore, the predicted solution and flow evolution should closely follow the true physics in flow conditions considered at a very high Reynolds number. It is therefore legitimate for us to solve the computationally more difficult flow equations cast in the velocity–pressure primitive-variable form.

Numerical simulation of multidimensional incompressible Navier-Stokes equations at high Reynolds numbers normally encounters several major computational difficulties. One class of computational difficulties is associated with the approximation of the nonlinear convection terms which dominate the diffusion terms. Convective terms involve nonlinear first-order spatial derivative terms. As a result, a proper approximation of the convective terms needs, in addition to an effective linearization, consideration the upwind nodal solutions along the flow direction. This means that the underlying methodology that enables minimization of the phase error for the flow direction–relevant first-order spatial terms is desired. This motivates the current development of an upwinding scheme which underlies the Fourier transform. Another instability problem occurring in the simulation of incompressible fluid flows in colocated grids is due to the presence of an even–odd pressure mode. To resolve these nonphysical oscillations in the pressure field, we are motivated to develop a center-type compact scheme to approximate the pressure gradient term in the programmably more simple nonstaggered grids. Application of upwinding schemes to approximate advective terms will inevitably introduce false diffusion error for flow problems involving more than one spatial dimension. For the sake of prediction accuracy, we will develop a high-order compact scheme for the spatial derivative terms in a grid stencil containing only a few nodal points.

The other topic, less explored in the past, which we will address in this article is the time integrator chosen for the approximation of the temporal derivative term in the equations of motion for the incompressible fluid flow investigated at a very high Reynolds number. One can easily apply any high-order time-stepping scheme in the literature to calculate the Navier-Stokes solution. When one desires a long-time accurate solution for the incompressible viscous fluid flow at high Reynolds

numbers, however, attention needs to be paid to the time-stepping scheme chosen. The main reason is that the time derivative term with respect to the source terms, which are $-\nabla p$, $1/Re\nabla^2 \underline{u}$, and the inertia term $(\underline{u}\cdot\nabla)\underline{u}$ in the momentum equations, plays different roles, particularly, when the fluid viscosity is very close to zero. In this limiting case, the equations of motion, subject to the divergence-free constraint condition, have been classified as a nonlinear Hamiltonian differential system. Under these circumstances, a legitimate time integrator must be applied to retain both the Hamiltonian and the Casimir embedded in the incompressible inviscid Euler equations [2]. In this light, we are motivated in the present study, which is aimed at simulating the incompressible flow at high Reynolds numbers, to rigorously solve the momentum equations in time and enforce the continuity equation in separate steps. The key to success in the proposed projection (or fractional-step) method is that the time integrator with the symplectic property will be applied to solve the equation involving the Hamiltonian structure. In the diffusion step, one can apply an integrator which is either symplectic or nonsymplectic, since there exists no Hamiltonian system for any flow equation with a damping term. The theorem in support of the splitting of equations is known as the Clebsch velocity decomposition [3], which bears a similarity to the well-known Hodge decomposition of the velocity vector in the incompressible Navier-Stokes equations.

The rest of this article is organized as follows. In Section 2 we present the working incompressible Navier-Stokes equations in primitive-variable form and the theoretical foundations that will be applied to the case with a vanishing viscosity. In Section 3 the three-step iterative solution algorithm is presented so that one can apply mathematically plausible time-stepping schemes for solving the corresponding equations in each fractional step. We then present the discretization schemes, in Sections 4 and 5, for the spatial and temporal derivative terms, by which both the solution accuracy and the scheme stability can be assured. In Section 6, five benchmark problems are investigated to justify the proposed discretization scheme and solution algorithm. Attention to the calculation of a long-time accurate solution is specifically addressed in the result section. Finally, we make draw some concluding remarks in Section 7.

2. GOVERNING EQUATIONS IN PRIMITIVE AND CLEBSCH VARIABLES

We consider the following Navier-Stokes equations cast in primitive variables $\underline{u}$ and p for modeling the motion of an incompressible viscous fluid flow:

$$\frac{\partial \underline{u}}{\partial t} + (\underline{u}\cdot\nabla)\underline{u} = -\nabla p + \frac{1}{\mathrm{Re}}\nabla^2 \underline{u} \tag{1}$$

$$\nabla \cdot \underline{u} = 0 \tag{2}$$

In the above, $(\underline{u}, p)$ (velocity vector, pressure) is the chosen pair of working variables and Re the control parameter of the nonlinear dynamical system under current investigation. The above parabolic-elliptic differential system will be solved subject to a divergence-free initial velocity specified along the domain boundary. In the limit of vanishing viscosity, the above system of equations turns out to be the continuity equation (2) and the following incompressible Euler equations, which govern the

transport of velocity vector $\underline{u}$

$$\frac{\partial \underline{u}}{\partial t} + (\underline{u} \cdot \nabla)\underline{u} = -\nabla p \tag{3}$$

Analysis of the Euler flow equations (2)–(3) for an incompressible fluid flow, while having been known for more than 200 years, remains still a mathematically and computationally challenging academic issue in terms of solution regularity and singularity, which are closely related to the onset or the intermittency phenomena of turbulence [4]. Some rich geometric structures are also known to exist in the above incompressible Euler differential system. For example, the velocity vector for Eqs. (2)–(3) investigated in the two-dimensional domain can be expressed in terms of the Clebsch variables λ^i and μ^i ($i = 1, 2$) given below [3]:

$$\underline{u}(\underline{x}, t) = -\nabla\phi + \sum_{i=1}^{2} \lambda^i \nabla \mu^i \tag{4}$$

The scalar function $\phi(\underline{x}, t)$ shown above is determined by $\nabla \cdot \underline{u} = 0$. It is interesting to remark here that this Clebsch velocity decomposition shares a similarity to the Hodge decomposition, which shows that the velocity vector on the right-hand side of Eq. (4) can be decomposed into a divergence-free part and a gradient of scalar potential for the velocity [5].

It is also worth mentioning that the two Clebsch variables λ^i and μ^i are the Lagrangian invariants. As a result, their values remain unchanged along the fluid particle trajectories. In other words, the Clebsch variables for an incompressible flow follow the following transport equations:

$$\frac{\partial \lambda^i}{\partial t} + (\underline{u} \cdot \nabla)\lambda^i = 0 \tag{5}$$

$$\frac{\partial \mu^i}{\partial t} + (\underline{u} \cdot \nabla)\mu^i = 0 \tag{6}$$

One can therefore regard these Clebsch variables as the markers of vortex lines. Given the above Clebsch velocity decomposition [6], the vorticity field turns out to be $\omega = \nabla\lambda \times \nabla\mu$. Thanks to the Clebsch decomposition defined above for the velocity field $\underline{u}$, one can replace the differential equations (1)–(2) with the differential set of equations (5)–(6) and the following pressure field:

$$p = \left(\frac{\partial \phi}{\partial t} + \lambda^i \frac{\partial \mu^i}{\partial t} + \frac{1}{2}\underline{u} \cdot \underline{u} \right) \tag{7}$$

Owing to the introduction of the Clebsch variables, one can rewrite Eq. (3) in its canonical Hamiltonian form as [7, 8]

$$\frac{\partial \lambda^i(\underline{x}, t)}{\partial t} = \frac{\delta H}{\delta \mu^i(\underline{x}, t)} \tag{8}$$

$$\frac{\partial \mu^i(\underline{x}, t)}{\partial t} = -\frac{\delta H}{\delta \lambda^i(\underline{x}, t)} \tag{9}$$

where the Hamiltonian H, which physically represents the kinetic energy, is given by

$$H = \frac{1}{2}\int \underline{u} \cdot \underline{u} d\Omega \tag{10}$$

It is now known from Eqs. (8)–(10) that the incompressible Euler equations (1)–(2) fall into the category of Hamiltonian equations. This theoretical fact indicates that it is better to retain the symplectic property as often as possible when solving the incompressible Navier-Stokes equations.

It is important to address here that the scalar function ϕ shown in (4) plays a role like the velocity potential in a rotation-free flow. Under this irrotational condition, one can easily get $\nabla^2\phi = 0$, thanks to the divergence-free constraint condition given in Eq. (2). In other words, the first term in the Clebsch velocity representation [in Eq. (4)] accounts for the velocity due to flow irrotationality, while the second term, which involves Clebsch variables, is responsible for the creation of flow rotation. Note that the Clebsch representation of a velocity vector can be also found in the inviscid compressible flow field, where the rotational contribution has been shown to be identical to

$$\frac{1}{\gamma - 1}\frac{s}{C_v}\nabla \mu^i$$

where γ, C_v, and s represent the specific heat ratio, specific heat at constant volume, and entropy, respectively.

In light of the above, we see that the velocity vector in an incompressible fluid flow can be decomposed into three components due to velocity potential, flow rotation, and fluid viscosity. We can therefore view the dissipative system of Eqs. (1)–(2) as the transport of a lossless Euler flow system, governed by Eqs. (2)–(3), in a flow field containing fluid viscosity. This velocity decomposition forms the underlying theory of the proposed three-step solution algorithm, which will be given in the following section, for developing a mathematically rigorous and computationally effective Navier-Stokes flow solver for Eqs. (1)–(2).

THREE-STEP ITERATIVE SOLUTION ALGORITHM

In addition to machine error, any numerical simulation of Eqs. (1)–(2) will introduce dispersive and dissipative errors when approximating the derivative terms. In addition to the consistency and stability requirements, a computationally proper and reliable simulation also demands satisfaction of some conserved properties at all times, such as the Hamiltonian and Casimir embedded in the viscosity-free differential system, and the divergence-free constraint condition in the flow field.

For stability, we will eliminate the notorious even–odd pressure oscillations computed from Eqs. (1)–(2) in nonstaggered grids and suppress velocity oscillations in cases when the convection effect dominates its diffusion counterpart. It is also

imperative that the solution computed from the momentum equation, given in (1), for an incompressible fluid flow must be divergence-free within the discrete context.

As the Reynolds number in Eq. (1) becomes increasingly large, the elliptic-parabolic differential system (1)–(2) approaches more and more to the incompressible Euler differential system, shown in (2)–(3), which possesses several Hamiltonian properties. The implication under these circumstances is that the approximation of time derivative terms in Eq. (1) warrants special care so as to retain the symplectic property embedded in the differential system as Re becomes infinitely large.

To retain a long-time accurate solution when solving the Eqs. (1)–(2) at high Reynolds numbers, we propose a three-step solution algorithm based on the Clebsch velocity decomposition presented in Section 2. Given the solutions for $\underline{u}$ and p at $t^n = n\,\Delta t$, these primitive variables at $t^{n+1} = (n+1)\,\Delta t$ will be calculated iteratively from the following Marchuk-Yanenko fractional-step solution algorithm [9].

Step 1. Convection step. Specify $\underline{u}(\underline{x},\ t = n\,\Delta t)$ as $\overline{\underline{u}}$ so as to linearize the differential system given below for $\underline{u}^*$ and p^*in a domain with boundary Γ

$$\frac{\partial \underline{u}^*}{\partial t} + (\overline{\underline{u}} \cdot \nabla)\underline{u}^* = 0 \tag{11}$$

where $\underline{u}^*|_{t=t^n} = \underline{u}^n$.

Step 2. Diffusion step

$$\frac{\partial \underline{u}^{**}}{\partial t} = \frac{1}{\mathrm{Re}} \nabla^2 \underline{u}^{**} \tag{12}$$

where $\underline{u}^{**}|_{t=t^n} = \underline{u}^*|_{t=t^{n+1}}$.

Step 3. Projection step

$$\frac{\partial \underline{u}^{***}}{\partial t} = -\nabla p^* \tag{13}$$

where $\underline{u}^{***}|_{t=t^n} = \underline{u}^{**}|_{t=t^n}$.

$$\frac{\underline{u}^{n+1} - \underline{u}^{***}}{\Delta t} = -\nabla p' \tag{14}$$

$$\nabla \cdot \underline{u}^{n+1} = 0 \tag{15}$$

or

$$\nabla^2 p' = \tfrac{1}{\Delta t} \nabla \cdot \underline{u}^{***} \tag{16}$$

$$\underline{n} \cdot \nabla p'|_{\Gamma} = 0 \tag{17}$$

The updated value of $\underline{u}$ can be calculated from

$$\underline{u}^{n+1} = \underline{u}^{***} - \Delta t \nabla p' \tag{18}$$

The solution algorithm is summarized below:

($A1$) Guess the initial values for u^* and p^*.
($A2$) Solve Eq. (11) to get the velocity vector $\underline{u}^*|_{t=t^{n+1}}$.
($A3$) Solve Eq. (12) to get the velocity vector $\underline{u}^{**}|_{t=t^{n+1}}$.
($A4$) Solve Eq. (13) to get the velocity vector $\underline{u}^{***}|_{t=t^{n+1}}$.
($A5$) Solve Eq. (16) to get the value of p' and the updated velocity vector $\underline{u}^{n+1}$ by solving Eq. (18).
($A6$) Check whether the tolerance, defined as $\underline{u}^{n+1} - \underline{u}^*$, reaches the user's specified value, which is se as 10^{-6} in the present study. If convergence is reached, then exit; otherwise, update the pressure value by virtue of $p^*_{s+1} = p^*_s + p'_s$ and set $u^*_{s+1} = u^{n+1}$ to repeat steps ($A1$)–($A5$).

It is important to address that the time integrator in Eq. (11) can be different from that in Eq. (12) in the diffusion step. The reason for employing a symplectic time integrator for Eq. (11) is to preserve its well-known conserved quantities.

4. SYMPLECTIC DISCRETIZATION SCHEME FOR THE TIME DERIVATIVE TERMS

In this study we discretize the time derivative term, which will be described in this section, to preserve its embedded symplecticity. The resulting ordinary differential equation will then be approximated in space by the method detailed in Section 5 to minimize the phase error for the first-order spatial derivative terms.

The following linearized equation for (11) will be used to describe the proposed method, where $\overline{\underline{u}}$ is assumed to be a real-valued constant:

$$\underline{u}_t = -(\overline{\underline{u}} \cdot \nabla)\underline{u} \tag{19}$$

A proper time-stepping scheme should be employed in the current semidiscretization method so that the Hamiltonian structure embedded in the above differential equation can be retained all the time [2]. Let $\underline{F} = -(\overline{\underline{u}} \cdot \nabla)\underline{u}$ be sufficiently differentiable; then Eq. (19) can be rewritten as $\underline{u}_t = \underline{F}(\overline{\underline{u}}, \nabla\underline{u})$. In the present study, we apply the sixth-order-accurate symplectic Runge-Kutta scheme in [10] to preserve the symplecticity in Eq. (19) at each time step.

Given the time-accurate solution $\underline{u}^n$ at $t = n\,\Delta t$, we will calculate $\underline{u}^{n+1}$ by marching the calculation with a time step Δt using the following iterative method. We start with the guessed values $\underline{u}^{(i)}$ for $\underline{u}^n$, where $i = 1$–3, and then calculate the values of $\underline{F}^{(i)}$. This is followed by substituting $\underline{F}^{(i)}(i = 1\text{–}3)$ into the following three equations to get the updated values of $\underline{u}^{(i)}(i = 1 \text{ to } 3)$:

$$\underline{u}^{(1)} = \underline{u}^n + \Delta t\left[\frac{5}{36}\underline{F}^{(1)} + \left(\frac{2}{9} + \frac{2\widetilde{c}}{3}\right)\underline{F}^{(2)} + \left(\frac{5}{36} + \frac{\widetilde{c}}{3}\right)\underline{F}^{(3)}\right] \tag{20}$$

$$\underline{u}^{(2)} = \underline{u}^n + \Delta t\left[\left(\frac{5}{36} - \frac{5\widetilde{c}}{12}\right)\underline{F}^{(1)} + \frac{2}{9}\underline{F}^{(2)} + \left(\frac{5}{36} + \frac{5\widetilde{c}}{12}\right)\underline{F}^{(3)}\right] \tag{21}$$

$$\underline{u}^{(3)} = \underline{u}^n + \Delta t\left[\left(\frac{5}{36} - \frac{\widetilde{c}}{3}\right)\underline{F}^{(1)} + \left(\frac{2}{9} - \frac{2\widetilde{c}}{3}\right)\underline{F}^{(2)} + \frac{5}{36}\right] \tag{22}$$

where $\widetilde{c} = \frac{1}{2}\sqrt{\frac{3}{5}}$ and $d\underline{u}/dt = \underline{F}(\underline{u})$. Note that $F^{(i)}(i = 1\text{–}3)$ represents the values of $\underline{F}$ evaluated at $t = n + (\frac{1}{2} + \widetilde{c})\Delta t$, $t = n + \frac{1}{2}\Delta t$, and $t = n + (\frac{1}{2} - \widetilde{c})\Delta t$, respectively. Before the computed difference of $\underline{u}^{(i)}$ between each two iterations becomes negligibly small, we continue the calculation of $\underline{F}^{(i)}$ according to Eqs. ((20)–(22). Upon reaching the user's specified tolerance, we can calculate the solution at the time $(n+1)\Delta t$ from the following equation:

$$\underline{u}^{n+1} = \underline{u}^n + \Delta t\left(\frac{5}{18}\underline{F}^{(1)} + \frac{4}{9}\underline{F}^{(2)} + \frac{5}{18}\underline{F}^{(3)}\right) \tag{23}$$

Note that the computed solution $\underline{u}$ from Eq. (19) using the above proposed time-stepping scheme preserves symplecticity provided that $(\underline{\overline{u}} \cdot \nabla)\underline{u}$ is computed exactly. To get as accurate a result as possible, the right-hand side of Eq. (19) motivates the development of the optimized upwinding approximation of the term $\nabla \underline{u}$ in Section 5. In all the test problems we have conducted, the tolerance was chosen to be 10^{-7} in the implicit calculation of $u^{(1)}$, $u^{(2)}$, and $u^{(3)}$ in Eqs. (20)–(22).

5. DEVELOPMENT OF A COMBINED COMPACT SCHEME WITH MINIMIZED PHASE ERROR FOR THE SPATIAL DERIVATIVE TERMS

The first-order derivative term, for example, in Eq. (11) or (19), and the second-order derivative term, for example, in Eq. (12), will be approximated within the following three-point compact framework [11]:

$$a_1 \left.\frac{\partial u}{\partial x}\right|_{i-1} + \left.\frac{\partial u}{\partial x}\right|_i = \frac{1}{h}(c_1 u_{i-1} + c_2 u_i + c_3 u_{i+1}) - h\left(b_1 \left.\frac{\partial^2 u}{\partial x^2}\right|_{i-1} + b_2 \left.\frac{\partial^2 u}{\partial x^2}\right|_i + b_3 \left.\frac{\partial^2 u}{\partial x^2}\right|_{i+1}\right) \tag{24}$$

$$\overline{b}_1 \left.\frac{\partial^2 u}{\partial x^2}\right|_{i-1} + \left.\frac{\partial^2 u}{\partial x^2}\right|_i + \overline{b}_3 \left.\frac{\partial^2 u}{\partial x^2}\right|_{i+1} = \frac{1}{h^2}(\overline{c}_1 u_{i-1} + \overline{c}_2 u_i + \overline{c}_3 u_{i+1}) - \frac{1}{h}\left(\overline{a}_1 \left.\frac{\partial u}{\partial x}\right|_{i-1} + \overline{a}_2 \left.\frac{\partial u}{\partial x}\right|_i + \overline{a}_3 \left.\frac{\partial u}{\partial x}\right|_{i+1}\right) \tag{25}$$

The derivative terms $\partial u/\partial y$ and $\partial^2 u/\partial y^2$ along the y direction be similarly approximated as $\partial u/\partial x$ and $\partial^2 u/\partial x^2$. Note that the compact schemes for $\partial u/\partial x|_i$ and $(\partial^2 u/\partial x^2)|_i$ at the nodal point i are coupled through the terms $(\partial u/\partial x)|_{i-1}$, $\partial u/\partial x|_i$, $\partial u/\partial x|_{i+1}$, $\partial^2 u/\partial x^2|_{i-1}$, $\partial^2 u/\partial x^2|_i$, $\partial^2 u/\partial x^2|_{i+1}$, u_{i-1}, u_i, u_{i+1}. For the sake of description, we consider the case involving only the positive convective coefficient. As for the case with the negative convective coefficient, the derivation will be the same.

The approximation error for $\partial^2 u/\partial x^2$ is normally classified to be dissipative. For this reason, the weighting coefficients shown in Eq. (25) will be determined solely

by the modified equation analysis to get higher spatial accuracy. Along the line of this thought, we can derive the coefficients in Eq. (25) as $\bar{a}_1 = -\frac{9}{8}, \bar{a}_2 = 0, \bar{a}_3 = \frac{9}{8}$, $\bar{b}_1 = -\frac{1}{8}, \bar{b}_3 = -\frac{1}{8}, \bar{c}_1 = 3, \bar{c}_2 = -6$, and $\bar{c}_3 = 3$. Use of this set of derived coefficients can render the following modified equation for $\partial^2 u/\partial x^2$ with spatial accuracy order of 6:

$$\frac{\partial^2 u}{\partial x^2} = \frac{\partial^2 u}{\partial x^2}\bigg|_{\text{exact}} + \frac{h^6}{20,160}\frac{\partial^8 u}{\partial x^8} + \frac{h^8}{604,800}\frac{\partial^{10} u}{\partial x^{10}} + O(h^{12}) + \dots$$

for the coefficients a_1, b_1 to b_3 and c_1 to c_3, they are determined partly by applying the Taylor series expansions for $u_{i\pm1}$, $\partial u/\partial x|_{i-1}$ and $\partial^2 u/\partial x^2|_{i\pm1}$ with respect to u_i, $\frac{\partial u}{\partial x}|_i$ and $\frac{\partial^2 u}{\partial x^2}|_i$. Derivation of the introduced coefficients is followed by eliminating the leading error terms shown in the modified equation, from which the following set of algebraic equations for Eq. (24) can be derived:

$$c_1 + c_2 + c_3 = 0 \tag{26}$$

$$-a_1 - c_1 + c_3 - 1 = 0 \tag{27}$$

$$-a_1 + b_1 + b_2 + b_3 - \frac{c_1}{2} - \frac{c_3}{2} = 0 \tag{28}$$

$$\frac{a_1}{2} - b_1 + b_3 + \frac{c_1}{6} - \frac{c_3}{6} = 0 \tag{29}$$

$$-\frac{a_1}{6} + \frac{b_1}{2} + \frac{b_3}{2} - \frac{c_1}{24} - \frac{c_3}{24} = 0 \tag{30}$$

$$\frac{a_1}{24} - \frac{b_1}{6} + \frac{b_3}{6} + \frac{c_1}{120} - \frac{c_3}{120} = 0 \tag{31}$$

We are now still short of one algebraic equation for us to uniquely determine the seven coefficients introduced in Eq. (24). To accurately approximate the first-order derivative term from Eq. (24), we will minimize the phase error by applying Fourier transform analysis.

The Fourier transform and its inverse for u, for example, given below, will be employed:

$$\tilde{u}(\alpha) = \frac{1}{2\pi}\int_{-\infty}^{+\infty} u(x)\ \exp(-\mathbf{i}\,\alpha x)\ dx \tag{32}$$

$$u(x) = \int_{-\infty}^{+\infty} \tilde{u}(\alpha)\ \exp(\mathbf{i}\,\alpha x)\ d\alpha \tag{33}$$

where $\mathbf{i}$ represents $\sqrt{-1}$. We then perform a Fourier transform on each term in Eqs. (24) and (25). The expressions of the actual wavenumber α for Eqs. (24) and

(25) can therefore be derived as

$$\begin{aligned}\mathbf{i}\alpha h[a_1\exp(-\mathbf{i}\alpha h)+1] \simeq c_1\exp(-\mathbf{i}\alpha h)+c_2+{}_3\exp(i\alpha h)\\ -(\mathbf{i}\alpha h)^2[b_1\exp(-\mathbf{i}\alpha h)+b_2+b_3\exp(i\alpha h)]\end{aligned} \tag{34}$$

and

$$\begin{aligned}(\mathbf{i}\alpha h)^2\left[-\frac{1}{8}\exp(-\mathbf{i}\alpha h)+1-\frac{1}{8}\exp(\mathbf{i}\alpha h)\right] \simeq 3\exp(-\mathbf{i}\alpha h)-6+3\exp(i\alpha h)\\ -\mathbf{i}\alpha h\left[-\frac{8}{9}\exp(-i\alpha h)+\frac{8}{9}\exp(i\alpha h)\right]\end{aligned} \tag{35}$$

The two effective wavenumbers α' and $\alpha'\prime$ given below are enforced to get the same expressions as the terms on the right-hand sides of Eqs. (34) and (35) to get an accurate phase prediction [12]:

$$\begin{aligned}\mathbf{i}\alpha' h[a_1\exp(-\mathbf{i}\alpha h]+1) = c_1\exp(-\mathbf{i}\alpha h)+c_2+c_3\exp(\mathbf{i}\alpha h)\\ -(\mathbf{i}\alpha'' h)^2[b_1\exp(-\mathbf{i}\alpha h)+b_2+b_3\exp(\mathbf{i}\alpha h)]\end{aligned} \tag{36}$$

$$\begin{aligned}\mathbf{i}\alpha' h\left[-\frac{8}{9}\exp(-\mathbf{i}\alpha h)+\frac{8}{9}\exp(\mathbf{i}\alpha h)\right] = 3\exp(-\mathbf{i}\alpha h)-6+3\exp(\mathbf{i}\alpha h)\\ -(\mathbf{i}\alpha'' h)^2\left[-\frac{1}{8}\exp(-\mathbf{i}\alpha h)+1-\frac{1}{8}\exp(\mathbf{i}\alpha h)\right]\end{aligned} \tag{37}$$

The expressions of α' and α'' can be derived as follows by solving Eqs. (36) and (37) simultaneously:

$$\begin{aligned}\alpha' h = -\mathbf{i}[&24b_1\exp(-2\mathbf{i}\alpha h)+c_1\exp(-2\mathbf{i}\alpha h)+c_3+c_1+24b_1+c_2\exp(-\mathbf{i}\alpha h)\\ &+24b_2\exp(-\mathbf{i}\alpha h)+24b_3-48b_1\exp(-\mathbf{i}\alpha h)-8c_1\exp(-\mathbf{i}\alpha h)\\ &-48b_3\exp(\mathbf{i}\alpha h)+24b_2\exp(\mathbf{i}\alpha h)+24b_3\exp(2\mathbf{i}\alpha h)-48b_2\\ &+c_2\exp(\mathbf{i}\alpha h)+c_3\exp(2\mathbf{i}\alpha h)-8c_3\exp(\mathbf{i}\alpha h)-8c_2]\\ /[&-8+\exp(\mathbf{i}\alpha h)-8a_1\exp(-\mathbf{i}\alpha h)+a_1\exp(-2\mathbf{i}\alpha h)-9b_1\exp(-2\mathbf{i}\alpha h)\\ &-9b_2\exp(-\mathbf{i}\alpha h)+9b_2\exp(\mathbf{i}\alpha h)+9b_3\exp(2\mathbf{i}\alpha h)+a_1+9b_1-9b_3+\exp(\mathbf{i}\alpha h)]\end{aligned} \tag{38}$$

$$\alpha'' h = \sqrt{-\frac{3\exp(-\mathbf{i}\alpha h)-6+3\exp(\mathbf{i}\alpha h)-\mathbf{i}\alpha' h\left[-\frac{8}{9}\exp(-\mathbf{i}\alpha h)+\frac{8}{9}\exp(\mathbf{i}\alpha h)\right]}{-\frac{1}{8}\exp(-\mathbf{i}\alpha h)+1-\frac{1}{8}\exp(\mathbf{i}\alpha h)}} \tag{39}$$

To get better dispersive accuracy for α', it is necessary that $\alpha h \approx \Re(\alpha' h)$, where $\Re(\alpha' h)$ denotes the real part of $\alpha' h$. This implies that $E(\alpha)$ defined below should be a small

positive value:

$$E(\alpha) = \int_{-\frac{\pi}{2}}^{\frac{\pi}{2}} \{W[\alpha h - \Re(\alpha' h)]\}^2 d(\alpha h) = \int_{-\frac{\pi}{2}}^{\frac{\pi}{2}} \{W[\gamma - \Re(\gamma')]\}^2 d\gamma \tag{40}$$

where $\gamma = \alpha h$ and $\gamma' = \alpha' h$. It is also noted that Eq. (40) can be analytically integrable provided that the weighting function W is chosen as

$$\begin{aligned} W = & -16 + 72b_3 + 72b_1 - 81b_1^2 - 81b_3^2 - 81b_2^2 \\ & - 162b_2b_3\cos(\gamma) - 144a_1b_3\cos(\gamma) - 162b_1b_2\cos(\gamma) \\ & - a_1^2\cos(\gamma)^2 + 8a_1^2\cos(\gamma) - 18b_3\cos(\gamma)^3 + 18b_1\cos(\gamma)^3 \\ & + 81b_2^2\cos(\gamma)^2 + 162b_1b_3 - 72b_1\cos(\gamma)^2 \\ & + 81b_3^2\cos(\gamma)^2 + 81b_1^2\cos(\gamma)^2 - 72a_1b_2 - 18b_1\cos(\gamma) \\ & + 16a_1\cos(\gamma)^2 - 2a_1\cos(\gamma)^3 + 72b_3\cos(\gamma)^2 \\ & + 18b_3\cos(\gamma) - 32a_1\cos(\gamma) - 36a_1b_3\cos(\gamma)^4 - 18a_1b_2\cos(\gamma)^3 + 162b_2b_3\cos(\gamma)^3 \\ & + 162b_1b_2\cos(\gamma)^3 + 324b_1b_3\cos(\gamma)^4 + 72a_1b_2\cos(\gamma)^2 + 144a_1b_3\cos(\gamma)^3 \\ & - 486b_1b_3\cos(\gamma)^2 + 36a_1b_3\cos(\gamma)^2 + 18a_1b_2\cos(\gamma) + 8\cos(\gamma) - 16a_1^2 - \cos(\gamma)^2 \end{aligned} \tag{41}$$

One should notice that the integration interval in Eq. (40) needs to be sufficiently large so as to be able to cover one complete sine (or cosine) wave.

To minimize the positive-valued fucntion defined in Eq. (40), the following extreme condition is enforced:

$$\frac{\partial E}{\partial c_3} = 0 \tag{42}$$

The above equation will be used together with the other six previously derived algebraic equations, by way of the modified equation analysis, to get higher accuracies in dissipation and in dispersion. Following this thought, the seven introduced unknowns can be uniquely determined as $a_1 = 0.875$, $b_1 = 0.12512823415990$, $b_2 = -0.24871765840091$, $b_3 = 0.00012823415990$, $c_1 = -1.93596119008109$, $c_2 = 1.99692238016218$, and $c_3 = -0.06096119008109$ [13]. The resulting upwind scheme for $\partial u/\partial x$ in three-grid stencil can be shown to have spatial accuracy order of 5 according to the modified equation derived below:

$$\begin{aligned} \frac{\partial u}{\partial x} = \left.\frac{\partial u}{\partial x}\right|_{\text{exact}} & - 0.00070085615243989224 75\, h^5 \frac{\partial^6 u}{\partial x^6} \\ & + 0.00019841269841269841 27\, h^6 \frac{\partial^7 u}{\partial x^7} \\ & - 0.00004988305074583303 90\, h^7 \frac{\partial^8 u}{\partial x^8} + O(h^8) + \ldots \end{aligned} \tag{43}$$

At the two boundary points x_1 and x_N, the following fourth-order-accurate one-sided boundary combined compact scheme can be similarly derived in a grid of three points:

$$\phi_1' + 2\phi_2' - h\phi_2'' = \frac{1}{h}(-3.5\phi_1 + 4\phi_2 - 0.5\phi_3) \tag{44}$$

$$h\phi_1'' + 5h\phi_2'' - 6\phi_2' = \frac{1}{h}(9\phi_1 - 12\phi_2 + 3\phi_3) \tag{45}$$

$$\phi_N' + 2\phi_{N-1}' + h\phi_{N-1}'' = \frac{1}{h}(3.5\phi_N - 4\phi_{N-1} + 0.5\phi_{N-2}) \tag{46}$$

$$h\phi_N'' + 5h\phi_{N-1}'' + 6\phi_{N-1}' = \frac{1}{h}(9\phi_N - 12\phi_{N-1} + 3\phi_{N-2}) \tag{47}$$

The three-point upwind combined compact scheme, which consists of Eqs. (44) and (45) for $i=1$, (46) and (47) for $i=N$, and Eqs. (24) and (25) for $i=2, 3, 4, \ldots, N-1$, formulates a $2N \times 2N$ matrix system, which can be effectively solved by the twin-tridiagonal solution solver.

6. NUMERICAL RESULTS

Having developed the combined compact scheme with minimized dispersion error, we will solve the pure advection problem in Section 6.1. We then apply the compact scheme together with the divergence-free-condition compensated viscous flow solver [14] to solve two steady-state problems in Sections 6.2 and 6.3 and then solve two unsteady problems in Sections 6.4 and 6.5.

6.1. Transport of a Gaussian Profile in an Inviscid Flow

To assess the proposed sixth-order symplectic Runge-Kutta (SRK6) scheme and the fourth-order symplectic Runge-Kutta (SRK4) [10] and conventional Runge-Kutta (RK4) [15] schemes, the problem with the smooth Gaussian profile $e^{(-\frac{(x+3)^2}{2}-\frac{(y+3)^2}{2})}$ for the equation $\phi_t + \underline{u}\nabla\cdot\phi = 0$ will be investigated in $-1 \le x \le 1$ and $-1 \le y \le 1$ with the prescribed velocity field $u=1$, $v=1$, and streamfunction $\psi = y - x$. Subject to the periodic boundary, the solutions will be calculated in 40×40 grids at time $t=270$. The Hamiltonian is defined as $H = \frac{1}{2}\int_\Omega \psi\phi d\Omega$. One can clearly see from Figure 1 that the symplectic Runge-Kutta schemes outperform the conventional Runge-Kutta scheme because of its ability to conserve the Hamiltonian. We also compare the required *CPU* times as tabulated in Table 1.

6.2. Two-Dimensional Lid-Driven Cavity Flow Problem

To verify the proposed discretization schemes, the flow driven by the constant upper lid velocity $u_{lid}(=1)$ in a square cavity is investigated at $\mathrm{Re}=400$, 1000, 5,000, and 7,500. The computed grid-independent mid-plane velocity profiles for $u(0.5, y)$ and $v(x, 0.5)$ are plotted for comparison sake. Good agreement between the

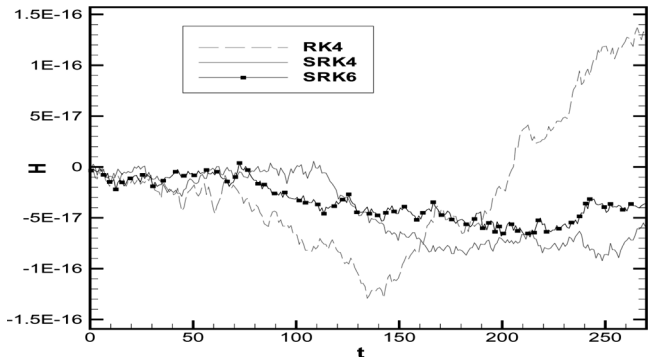

Figure 1. Predicted values of $H(\equiv=\frac{1}{2}\int_{\Omega}\psi\phi d\Omega)$, where H denotes the Hamiltonian, against the dimensionless time for the problem with a Gaussian profile moving in the domain of 40×40 nodal points.

predicted velocity and the benchmark solution of Ghia [17] can be clearly seen in Figure 2.

6.3. Natural Convection Problem

We also consider the energy equation that is coupled with the hydrodynamic equations through the buoyancy force. The resulting dimensionless divergence-free equation (2) and the two transport equations given below will be used together to predict the natural-convection phenomena in a gravitational field $\underline{g}=(0,\ -g)$:

$$\frac{\partial \underline{u}}{\partial t}+\underline{u}\cdot\nabla\underline{u}=-\nabla p+Pr\nabla^2\underline{u}+RaPrT\underline{e}_y \tag{48}$$

$$\frac{\partial T}{\partial t}+\underline{u}\cdot\nabla T=\nabla^2 T \tag{49}$$

Note that the parameters Ra $(\equiv\frac{g\beta\Delta TL^3}{\alpha\upsilon})$ and Pr $(\equiv\frac{\upsilon}{\alpha})$ are well known as the Rayleigh and Prandtl numbers, where υ, α and β denote, respectively, the kinematic viscosity, thermal diffusivity, and thermal expansion coefficient of the investigated fluid flow.

The classical natural-convection problem will be solved in a square at $\mathrm{Ra}=10^3$, 10^4, 10^5, 10^6, 10^7 and $Pr=0.71$. No-slip boundary condition is applied on the solid wall and the temperature boundary condition is specified as $\partial T/\partial y=0$ on the top

Table 1. Comparison of CPU-times required for solving pure advection equation in Section 6.1 using sixth-order symplectic Runge-Kutta (SRK6), fourth-order symplectic Runge-Kutta (SRK4), and fourth-order conventional Runge-Kutta (RK4) schemes

Method	CPU time (s)
Sixth-order symplectic Runge-Kutta (SRK6) scheme	6,556
Fourth-order symplectic Runge-Kutta (SRK4) scheme	3,979
Fourth-order conventional Runge-Kutta (RK4) scheme	2,307

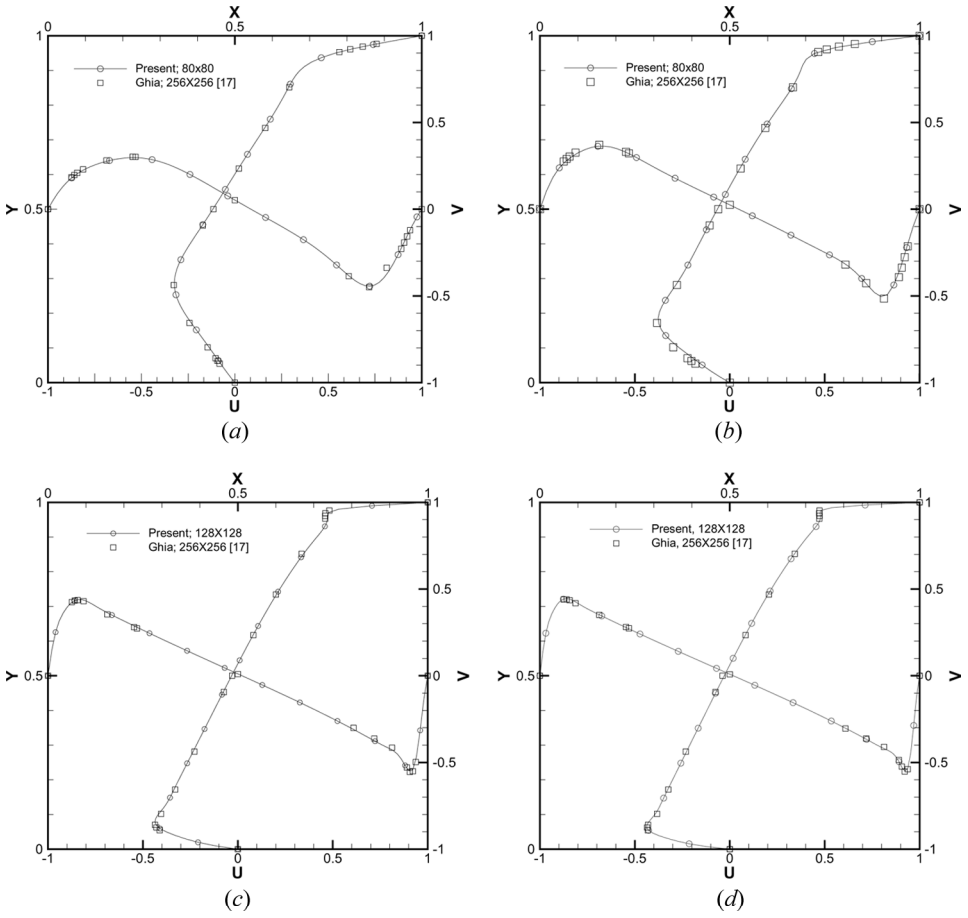

Figure 2. Comparison of predicted mid-plane velocity profiles $u(0.5, y)$ and $v(x, 0.5)$ for the lid-driven cavity flow problem investigated at different Reynolds numbers: (*a*) Re = 400; (*b*) Re = 1,000; (*c*) Re = 5,000; (*d*) Re = 7,500.

and bottom walls, $T = 1$ on the left hot wall, and $T = 0$ on the right cold wall. A uniform mesh with 80×80 nodal points is employed for the cases with $\mathrm{Ra} = 10^3$ and 10^4, and the nodal point is 128×128 for the cases with $\mathrm{Ra} = 10^5$, 10^6 and, 10^7. The predicted temperature solutions are plotted in Figure 3 for $\mathrm{Ra} = 10^6$ and $\mathrm{Ra} = 10^7$.

For the sake of of completeness, we also calculate the local Nusselt number Nu_x and its averaged value $\overline{Nu}$, which describe the heat transfer characteristics, in the cavity:

$$\mathrm{Nu}_x = \int_0^1 Q(x, y)dy \tag{50}$$

$$\overline{\mathrm{Nu}} = \int_0^1 \mathrm{Nu}_x dx \tag{51}$$

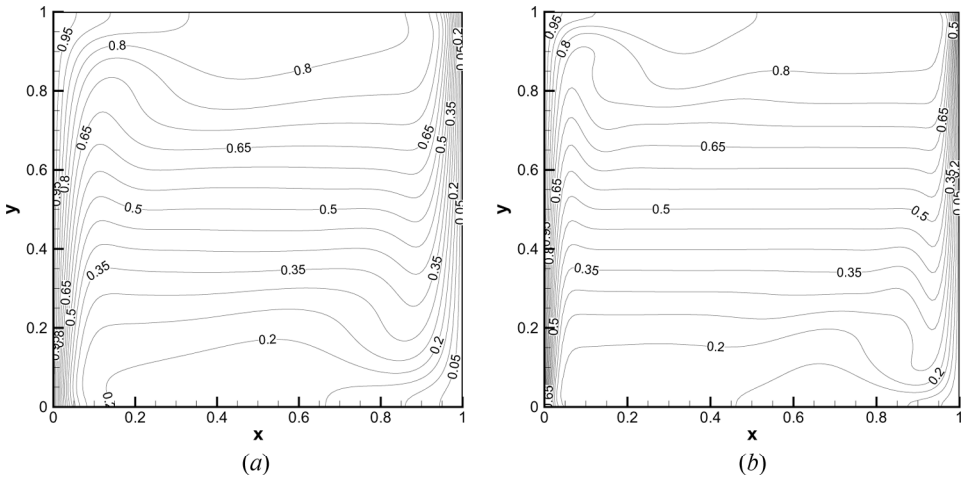

Figure 3. Computed temperature contours for the natural-convection problem investigated at different Rayleigh numbers: (*a*) $\mathrm{Ra} = 10^6$; (*b*) $\mathrm{Ra} = 10^7$.

where $Q(x, y) = uT - \partial T/\partial x$ is the local heat flux along the horizontal direction at any point in the cavity. One can see from Tables 2 and 3 that the predicted values of $v_{\max}$ and the averaged Nusselt number ($\overline{Nu}$) compare well with other simulated solutions given in [18–23].

6.4. Two-Dimensional Inviscid Double Jet Flow Problem

We apply the proposed symplecticity-preserving scheme to solve the incompressible flow equations, which are free of viscosity, in a domain without no-slip (or solid) walls. The resulting incompressible Euler equations given below in $0 \leq x$, $y \leq 2\pi$ are assumed to be periodic in both the x and y spatial directions:

$$\underline{u}_t + \underline{u} \cdot \nabla \underline{u} = -\nabla p \tag{52}$$

$$\nabla \cdot \underline{u} = 0 \tag{53}$$

Table 2. Comparison of computed values of $v_{\max}$ with other solutions

Ra	10^3	10^4	10^5	10^6	10^7
Kalita, Dalal, and Dass [18]	3.697	19.61	68.61	221.66	696.2
Chenoweth and Paolucci [19]	3.695	19.62	68.63	220.8	699.0
De Vahl Davis [20]	3.697	19.62	68.63	219.4	
Le Quéré [21]		19.63	68.64	220.46	
Hortmann, Peric and Scheure [22]				220.56	699.2
Ho and Lin [23]	3.697	19.63	68.63	219.86	705.3
Present work	3.698	19.63	68.60	220.78	699.5

Table 3. Comparison of computed values of $\overline{\mathrm{Nu}}$ with other solutions

Ra	10^3	10^4	10^5	10^6	10^7
Kalita, Dalal, and Dass [18]	1.118	2.245	4.522	8.829	16.52
Chenoweth and Paolucci [19]	1.118	2.244	4.520	8.822	16.82
De vahl Davis [20]	1.118	2.243	4.519	8.800	
Le Quéré [21]				8.825	16.52
Hortmann, Peric, and Scheure [22]		2.245	4.521	8.825	
Ho and Lin [23]	1.118	2.248	4.528	8.824	16.52
Present work	1.118	2.242	4.528	8.824	16.61

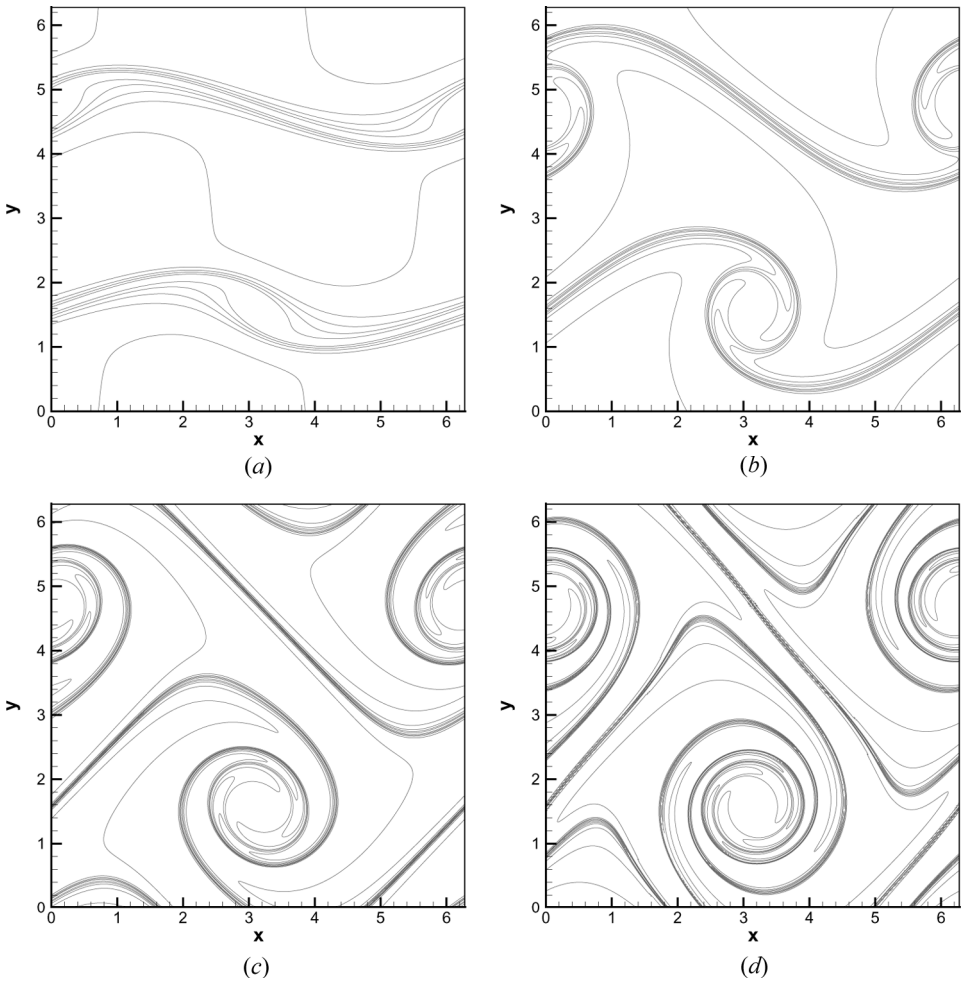

Figure 4. Computed iso-contours of vorticity in a domain of 512×512 grids at the four chosen times. The vorticity contour lines are drawn for every 0.1 dimensionless unit. (*a*) $t = 4$. (*b*) $t = 6$. (*c*) $t = 8$. (*d*) $t = 10$.

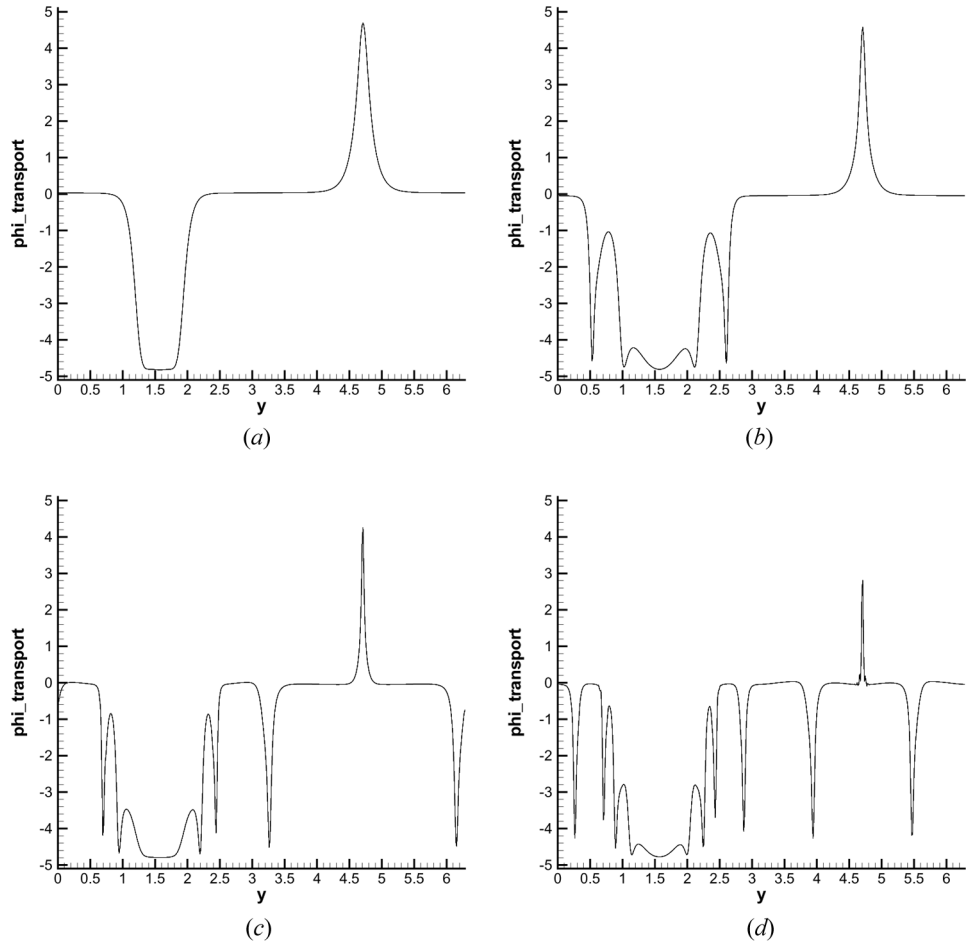

Figure 5. Predicted mid-sectional vorticity profiles of $\omega(\pi/2, y)$ in 512×512 grids at four different times: (*a*) $t = 4$; (*b*) $t = 6$; (*c*) $t = 8$; (*d*) $t = 10$.

The initial conditions for $\underline{u}(\equiv (u, v))$ and pressure p are prescribed below [24]:

$$u(x, y, t = 0) = \begin{cases} \tanh\left[\frac{y-\pi/2}{\delta}\right] & y \leq \pi \\ \tanh\left[\frac{3\pi/2-y}{\delta}\right] & y > \pi \end{cases}$$

$$v(x, y, t = 0) = \varepsilon \sin(x)$$

$$p(x, y, t = 0) = 0$$

In the above, the shear-layer thickness and the transverse perturbation parameter are set at $\delta = \pi/15$ and $\varepsilon = 0.05$, respectively. This problem, known as the double jet

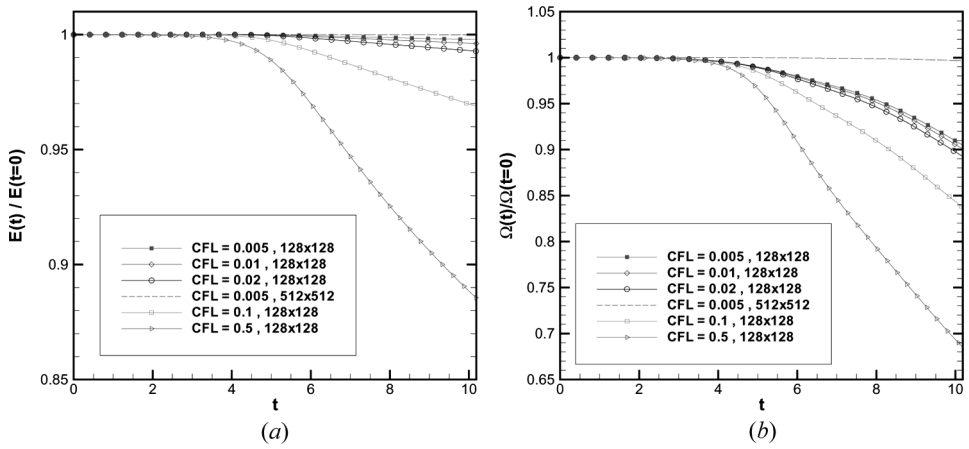

Figure 6. Predicted ratios of E $[\equiv E(t)/E(t=0)]$, where E denotes the kinetic energy defined in (54), and the ratio Ω $[\equiv \Omega(t)/\Omega(t=0)]$, where Ω is the enstrophy defined in (55), against the dimensionless time for the inviscid double jet flow problem investigated at different CFL numbers in the domain with 128×128 and 512×512 nodal points: (*a*) E; (*b*) Ω.

flow problem, has been considered as an ideal benchmark test to verify that the proposed advective scheme can be used to get a solution with high accuracy and good stability at high wavenumbers.

The double jet problem is solved at $\Delta t = 0.01\,\Delta x$ in a mesh of 512×512 nodal points. The computed iso-contours for the vorticity shown in Figure 4 at $t = 4$, $t = 6$, $t = 8$ and $t = 10$, are seen to agree well with other numerical solutions given in [24]. The predicted mid-sectional profiles for vorticity $\omega(\pi/2, y)$ are plotted in Figure 5 to show the sharply changed solution profiles.

To further justify the currently predicted solution, we plot three physically conserved quantities against time. Since the problem under current investigation is

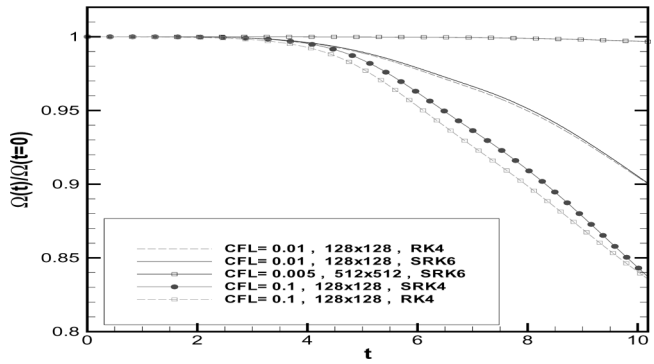

Figure 7. Predicted ratios of Ω $[\equiv \Omega(t)/\Omega(t=0))$, where Ω is the enstrophy defined in (55), against the dimensionless time for the inviscid double jet flow problem investigated at different CFL numbers using the sixth-order symplectic Runge-Kutta (SRK6) and fourth-order conventional Runge-Kutta (RK4) schemes.

Table 4. Comparison of CPU times for solving double jet problem in Section 6.4 using sixth-order symplectic Runge-Kutta (SRK6), fourth-order symplectic Runge-Kutta (SRK4), and fourth-order conventional Runge-Kutta (RK4) schemes

Method	CFL	Grids	CPU time (min)
Sixth-order symplectic Runge-Kutta (SRK6)	0.005	512×512	15486
Sixth-order symplectic Runge-Kutta (SRK6)	0.005	128×128	240
Sixth-order symplectic Runge-Kutta (SRK6)	0.01	128×128	150
Sixth-order symplectic Runge-Kutta (SRK6)	0.1	128×128	73
Sixth-order symplectic Runge-Kutta (SRK6)	0.5	128×128	176
Fourth-order symplectic Runge-Kutta (SRK4)	0.01	128×128	93
Fourth-order conventional Runge-Kutta (RK4)	0.01	128×128	53

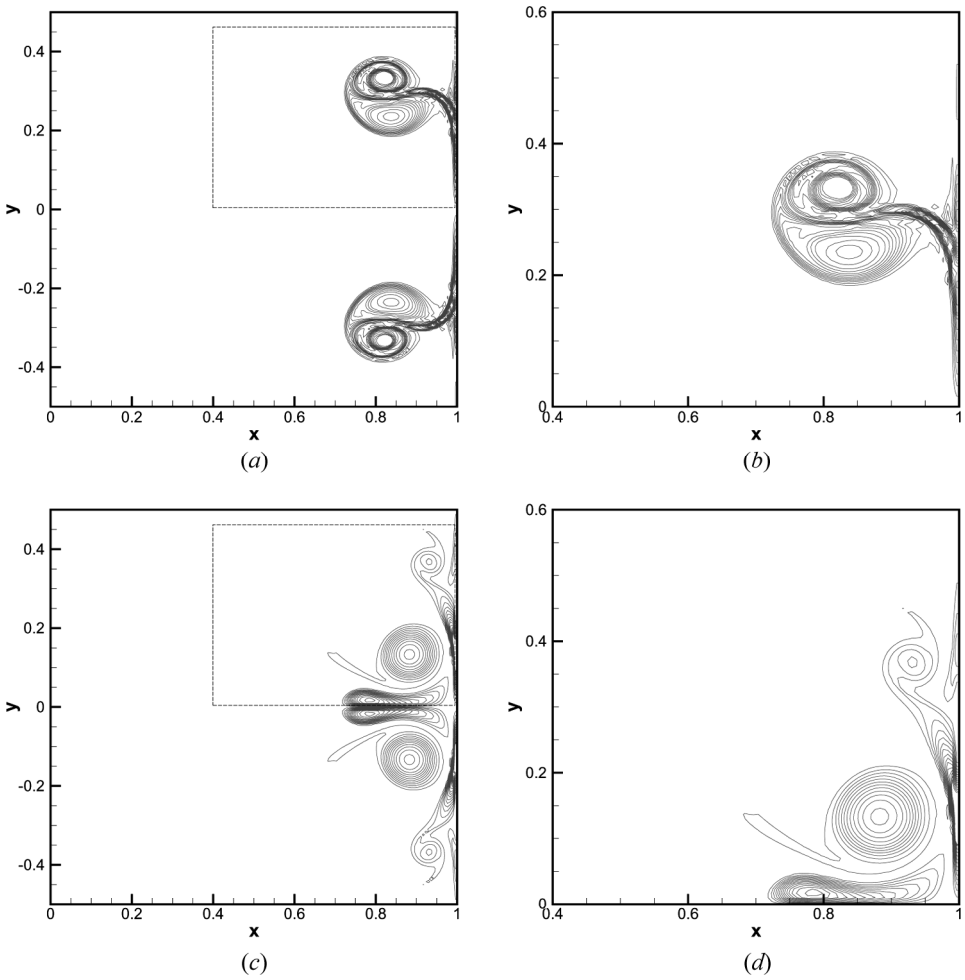

Figure 8. Predicted vorticity iso-contours in the domain of 768×768 grids. The vorticity contour lines at the four different times are drawn for every 20 dimensionless units. (*a*), (*b*) $t = 0.4$. (*c*), (*d*) $t = 0.6$. (*e*), (*f*) $t = 0.8$. (*g*), (*h*) $t = 1.0$. Note that (*b*), (*d*), (*f*), and (*h*) are the corresponding zoomed images of (*a*), (*c*), (*e*), and (*g*).

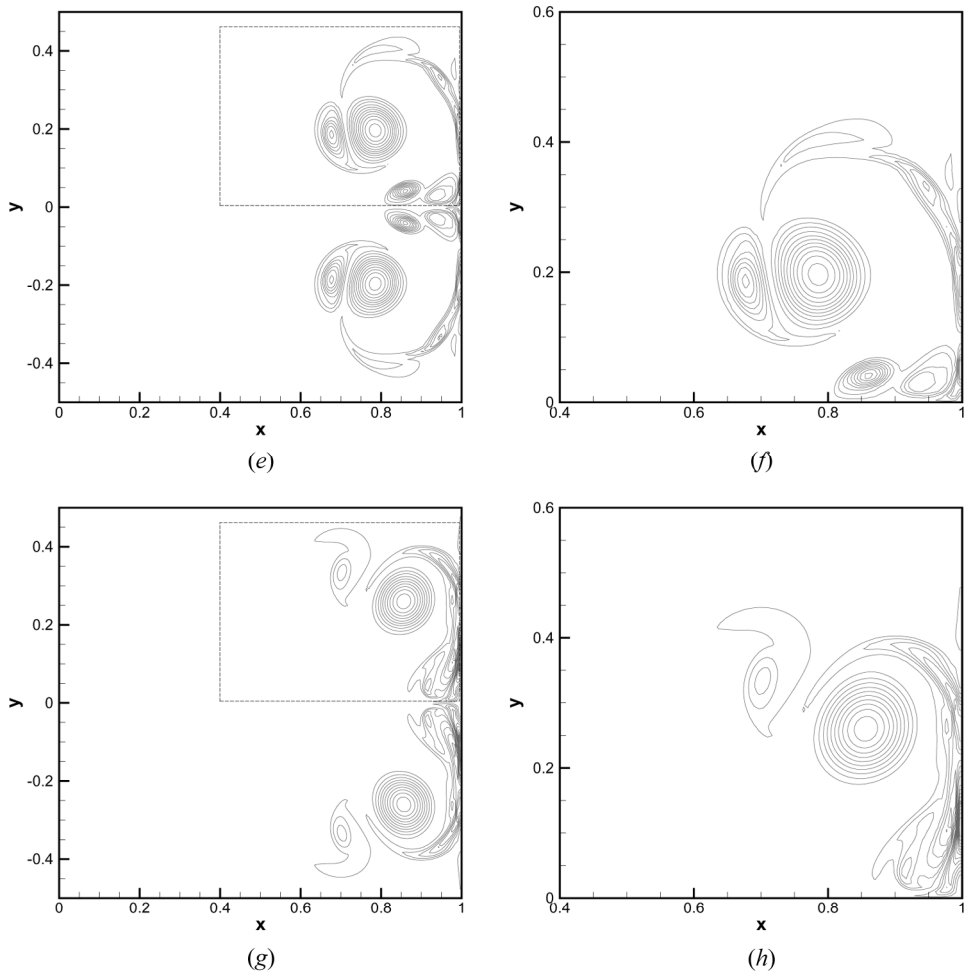

Figure 8 Continued.

free of viscosity and solid wall, the kinetic energy E and enstrophy Ω,

$$E = \frac{1}{2}\int_A \underline{u} \cdot \underline{u} dA \tag{54}$$

$$\Omega = \frac{1}{2}\int_A \omega^2 \, dA \tag{55}$$

are both conserved [2]. One can clearly see from Figure 6 that both the energy E and the enstrophy ω have the same values as their corresponding initial values using the proposed combined compact scheme at different CFL numbers. In addition, the computed values of the enstrophy ω are compared in Figure 7. Validation of the

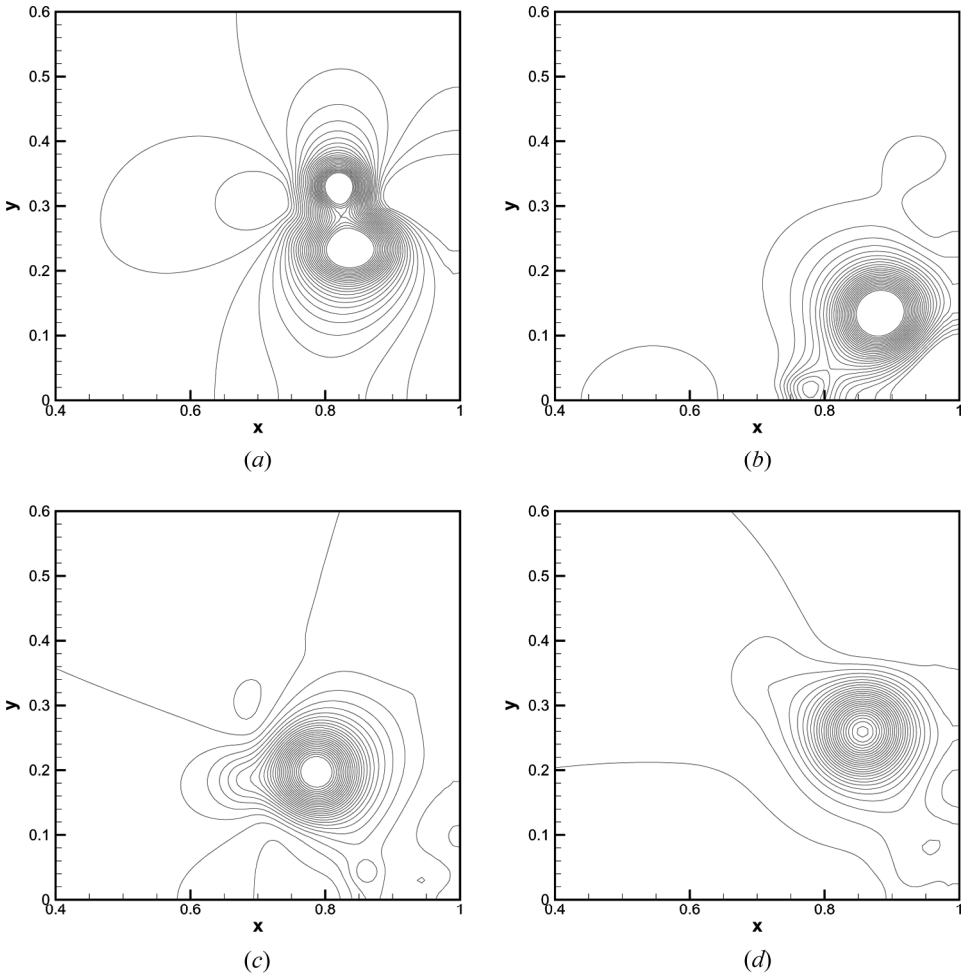

Figure 9. Predicted pressure iso-contours in the domain of 768×768 grids. The pressure contour lines at the four different times are drawn for every 1 dimensionless unit. (*a*) $t = 0.4$. (*b*) $t = 0.6$. (*c*) $t = 0.8$. (*d*) $t = 1.0$.

proposed inviscid Euler solver is therefore confirmed. The computational time is also tabulated in Table 4. To provide a rigorous justification of the proposed scheme, we may plot the value of H_e, where H_e ($\equiv \frac{1}{2}\int_D \underline{u} \cdot \underline{\Omega} d\Omega$), against time for the inviscid flow problem. The predicted total helicity remains zero, which is expected in the currently investigated two-dimensional problem.

6.5. Two-Dimensional Dipole-Wall Interaction Problem

A dipole–wall interaction problem [24] will be investigated next to also justify the proposed three-step incompressible viscous flow solver in the two-dimensional domain $-1 \leq x,\ y \leq 1$. Unsteady and viscous incompressible flow equations with the prescribed viscosity are solved subject to the following counterrotating vortices,

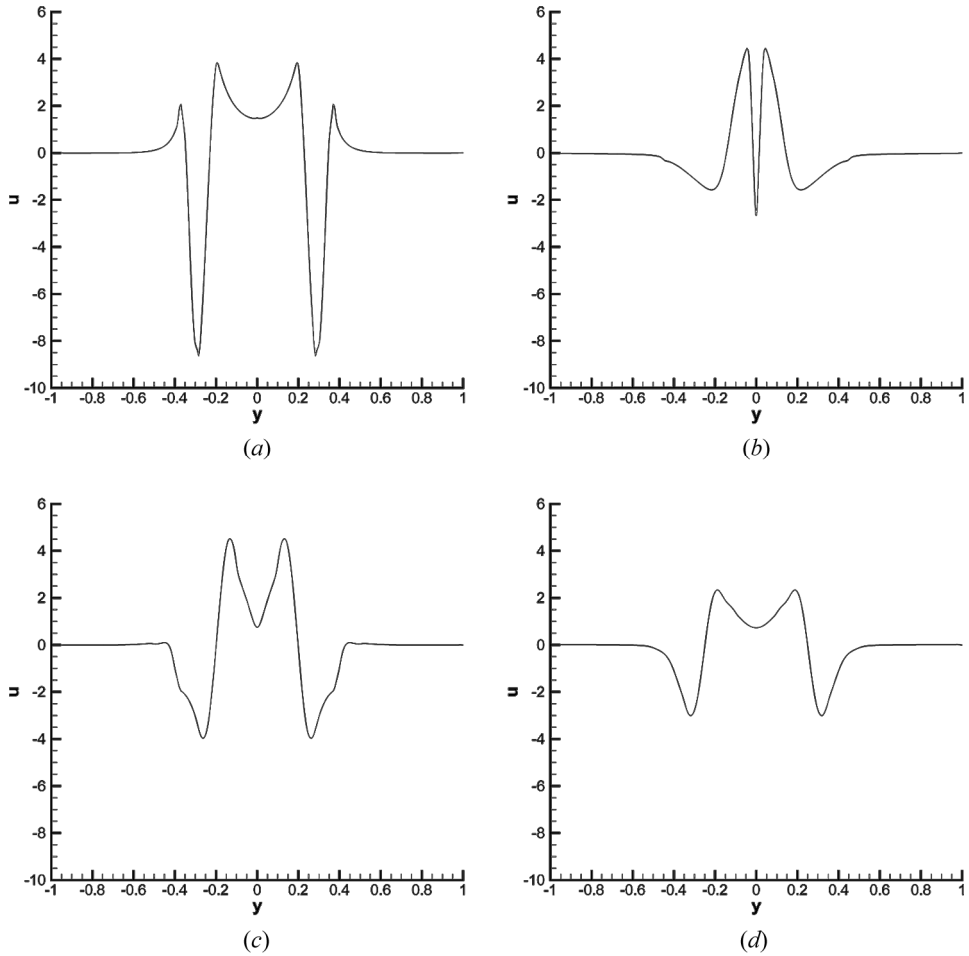

Figure 10. Predicted mid-sectional profiles of $u(0.8, y)$ in the domain of 768×768 grids at four different times: (*a*) $t = 0.4$; (*b*) $t = 0.6$; (*c*) $t = 0.8$; (*d*) $t = 1.0$.

which are located initially at (0, 0.1) and (0, -0.1):

$$u(x, y, 0) = \frac{1}{2}|\omega_e|\{-(y - y_1)\exp[-(r_1/r_0)^2] + (y - y_2)\ \exp[-(r_2/r_0)^2]\} \tag{56}$$

$$v(x, y, 0) = \frac{1}{2}|\omega_e|\{-(x - x_1)\exp[-(r_1/r_0)^2] + (x - x_2)\ \exp[-(r_2/r_0)^2]\} \tag{57}$$

$$p(x, y, 0) = 0 \tag{58}$$

In the above, $r_0 = 0.1$ and $r_i^2 = (x - x_i)^2 + (y - y_i)^2$ ($i = 1, 2$). Note that the initial total kinetic energy is 2, provided that the vortex strength is set at $|\omega_e| = 300$. Calculation is

carried out at $\mathrm{Re} = 2$, 500 in a square domain where no-slip condition is applied at $x = \pm 1$ and $y = \pm 1$.

The solutions, predicted at $\Delta x = \Delta y = 1/768$, in grids 768×768, show that the vortex dipoles in Figure 8 have been split into two, with one of the vortices propagating toward the boundary $x = 1$. Similar to the predicted results of Knikker [24], the collision of the right-running dipole with the vertical wall at $x = 1$ can cause a complex flow pattern to develop. The pressure contours are also plotted at $t = 0.4$, $t = 0.6$, $t = 0.8$, and $t = 1.0$ in Figure 9. In addition, the predicted mid-sectional profiles for u velocity $u(0.8, y)$ and v velocity $v(0.8, y)$ are plotted in Figures 10 and 11, respectively. Unlike the inviscid case, the kinetic energy $E = \frac{1}{2}\int_A \underline{u} \cdot \underline{u} dA$ and the enstrophy $\Omega = \frac{1}{2}\int_A \omega^2 dA$ plotted in Figure 12 no longer remain unchanged in this dissipative case.

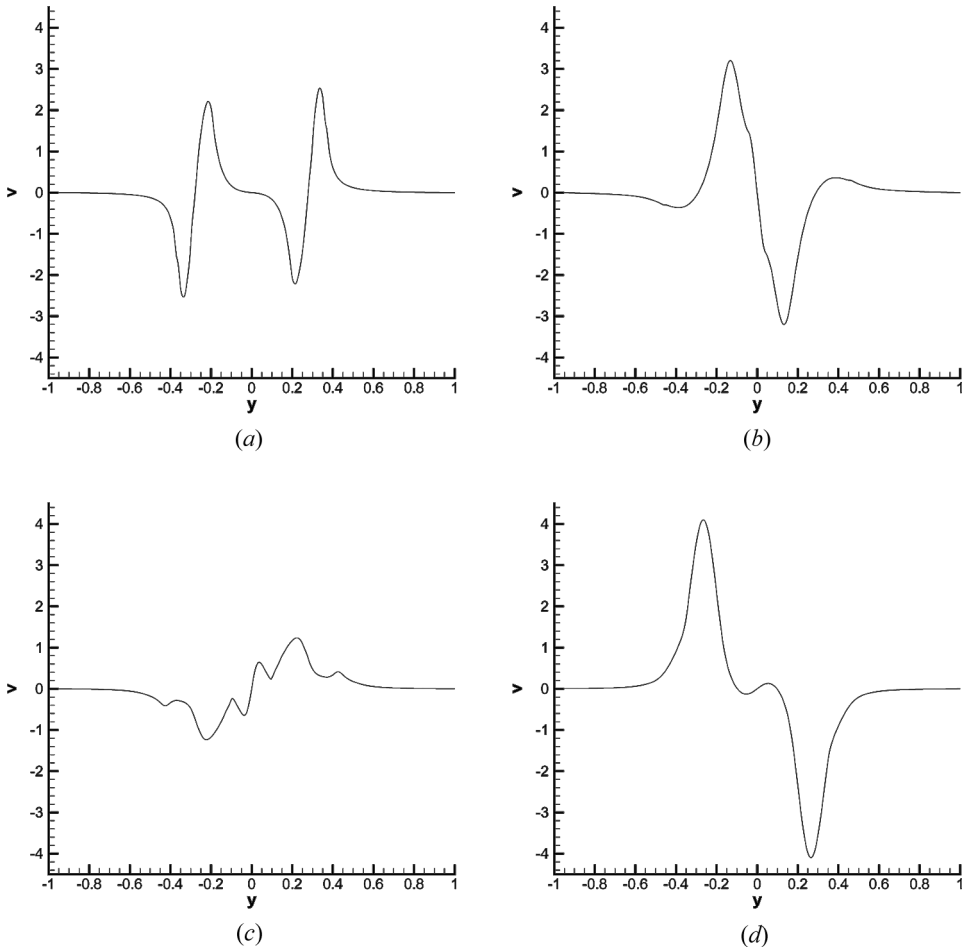

Figure 11. Predicted mid-sectional profiles of $v(0.8, y)$ in the domain of 768×768 grids at four different times: (*a*) $t = 0.4$; (*b*) $t = 0.6$; (*c*) $t = 0.8$; (*d*) $t = 1.0$.

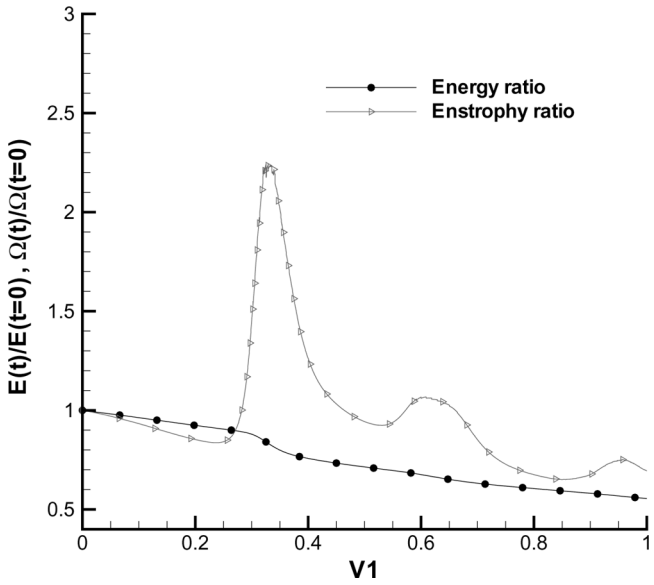

Figure 12. Predicted ratios of E [$\equiv E(t)/E(t=0)$], where E is the kinetic energy defined in (54), and Ω [$\equiv \Omega(t)/\Omega(t=0)$), where Ω denotes the enstrophy defined in (55), against the dimensionless time for the viscous dipole–wall problem investigated in the domain with 768×768 nodal points.

7. CONCLUDING REMARKS

Based on the underlying Clebsch velocity decomposition theory, we have decomposed the incompressible Navier-Stokes equations into the incompressible Euler equations and the scalar dissipative transport equation which is known as the time-dependent diffusion equation. The main advantage of applying the three-step fractional step splitting solution algorithm is that we can incorporate the properties of the Hamiltonian and Casimir, which are embedded in the Euler equations, into the current numerical formulation. The computed solution at a time after $t=0$ for a long time remains physically correct. For the sake of enhancing convective stability, the employed upwind scheme with fifth-order accuracy for the first-order spatial derivative term has been derived to minimize the phase error. In the pure advection solution step, which solves the incompressible Euler equations, two conservation laws have been numerically confirmed to exist by employing the temporal sixth-order-accurate symplectic Runge-Kutta scheme.

REFERENCES

1. L. Quartapella, *Numerical Solution of the Incompressible Navier-Stokes Equations*, ISNM vol. 113, Birkhäuser Verlag, Basel, 1993.
2. P. J. Morrison, Hamiltonian Description of the Ideal Fluid, *Rev. Mod. Phys.*, vol. 70, pp. 467–521, 1998.
3. W. Weber, Uber eine Transformation der hydrodynamischen Gleichungen, *J. Reine. Angew. Math.*, vol. 68, pp. 286–292, 1868.

4. K. Ohkitani, A Geometrical Study of 3D Incompressible Euler Flows with Clebsch Potentials— A Long-Lived Euler Flow and Its Power-Law Energy Spectram, *Physica D*, vol. 237, pp. 2020–2027, 2008.
5. A. J. Chorin, Numerical Solution of the Navier-Stokes Equations, *Math. Comput.*, vol. 22, pp. 745–762, 1968.
6. A. Clebsch, Uber die Integration der hydrodynamischen Gleichungen, *J. Reine. Angew. Math.*, vol. 56, p. 110, 1895.
7. G. Falkovich and V. S. Lvov, Isotropic and Anisotropic Turbulence in Clebsch Variables, *Chaos, Solitons and Fractals*, vol. 5, pp. 1855–1869, 1995.
8. H. Bateman, *Partial Differential Equations of Mathematical Physics*, Cambridge University Press, Cambridge, UK, 2003.
9. G. I. Marchuk, Splitting and Alternating Direction Methods, in *Handbook of Numerical Analysis*, vol. 1, pp. 197–462, North-Holland, Amsterdam, 1990.
10. W. Oevel and W. Sofroniou, Symplectic Runge-Kutta Schemes II: Classification of Symplectic Method, Univ. of Paderborn, Germany, Preprint, 1997.
11. P. C. Chu and C. Fan, A Three-Point Combined Compact Difference Scheme, *J. Comput. Phys.*, vol. 140, pp. 370–399, 1998.
12. C. K. W. Tam and J. C. Webb, Dispersion-Relation-Preserving Finite Difference Schemes for Computational Acoustics, *J. Comput. Phys.*, vol. 107, pp. 262–281, 1993.
13. P. H. Chiu and T. W. H. Sheu, On the Development of a Dispersion-Relation-Reserving Dual-Compact Upwind Scheme for Convection-Diffusion Equation, *J. Comput. Phys.*, pp. 3640–3655, 2009.
14. T. W. H. Sheu and P. H. Chiu, A Divergence-Free-Condition Compensated Method for Incompressible Navier-Stokes Equations, *Comput. Methods Appl. Mech. Eng.*, vol. 196, pp. 4479–4494, 2007.
15. J. D. Lambert, *Computational Methods in Ordinary Differential Equations*, Wiley, Chichester, UK, 1973.
16. O. A. Ladyzhenskaya, *The Mathematical Theory of Viscous Incompressible Flow*, Gordon & Breach, New York, 1969.
17. U. Ghia, K. N. Ghia, and C. T. Shin, High-Re Solutions for Incompressible Flow Using the Navier-Stokes Equations and a Multigrid Method, *J. Comput. Phys.*, vol. 48, pp. 387–411, 1982.
18. J. C. Kalita, D. C. Dalal, and A. K. Dass, Fully Compact Higher-Order Computation of Steady-State Natural Convection in a Square Cavity, *Phys. Rev. E*, vol. 64, pp. 1–13, 2001.
19. D. R. Chenoweth and S. Paolucci, Natural Convection in an Enclosed Vertical Air Layer with Large Horizontal Temperature Differences, *J. Fluid Mech.*, vol. 169, pp. 173–270, 1986.
20. G. de Vahl Davis, Natural Convection of Air in a Square Cavity: A Bench Mark Numerical Solution, *Int. J. Numer. Meth. Fluids*, vol. 3, pp. 249–264, 1983.
21. P. Le Quéré, Accurate Solutions to the Square Thermally Driven Cavity at High Rayleigh Number, *Comput. Fluids*, vol. 1, pp. 29–41, 1991.
22. M. Hortmann, M. Peric, and G. Scheuerer, Finite Volume Multigrid Prediction of Laminar Natural Convection: Benchmark Solutions, *Int. J. Numer. Meth. Fluids*, vol. 11, pp. 189–207, 1990.
23. C. J. Ho and F. H. Lin, Simulation of Natural Convection in a Vertical Enclosure by Using a New Incompressible Flow Formulation-Pseudovorticity-Velocity Formulation, *Numer. Heat Transfer A*, vol. 31, pp. 881–896, 1997.
24. R. Knikker, Study of a Staggered Fourth-Order Compact Scheme for Unsteady Incompressible Viscous Flows, *Int. J. Numer. Meths. Fluids*, vol. 48, pp. 387–411, 2008.